OPTICS

Realization of exceptional points along a synthetic orbital angular momentum dimension

Mu Yang[1,2]*, Hao-Qing Zhang[1,2]*, Yu-Wei Liao[1,2]*, Zheng-Hao Liu[1,2], Zheng-Wei Zhou[1,2,3], Xing-Xiang Zhou[1,2,3], Jin-Shi Xu[1,2,3]*, Yong-Jian Han[1,2,3]*, Chuan-Feng Li[1,2,3]*, Guang-Can Guo[1,2,3]

Exceptional points (EPs), at which more than one eigenvalue and eigenvector coalesce, are unique spectral features of non-Hermiticity (NH) systems. They exist widely in open systems with complex energy spectra. We experimentally demonstrate the appearance of paired EPs in a periodical-driven degenerate optical cavity along the synthetic orbital angular momentum dimension with a tunable parameter. The complex-energy band structures and the key features of EPs, i.e., their bulk Fermi arcs, parity-time symmetry breaking transition, energy swapping, and half-integer band windings, are directly observed by detecting the wavefront angle–resolved transmission spectrum. Our results demonstrate the flexibility of using the photonic synthetic dimensions to implement NH systems beyond their geometric dimension and EP-based sensing.

INTRODUCTION

The non-Hermiticity (NH) provides rich topology and unique physics distinct from the Hermitian system (1), among which the exceptional points (EPs) (2, 3) are prominent spectral features of NH systems. EPs are branch singularities in the momentum space of an NH system, where two or more eigenenergies and eigenstates simultaneously coalesce and become degenerate. They have been observed in extensive nonconservative systems exchanging energies with the environment (3–6). Many notable applications have been demonstrated for EP singularities, including the marked topological mode transport (6, 7), fractional topological charge measurement (8, 9), and ultrasensitive metrology (10, 11).

The EPs have been observed in two-dimensional (2D) or higher-dimensional geometric parameter spaces including solid single-spin systems (5, 12), acoustic cavities (4), microwave cavities (13, 14), or magnon polaritons (15). However, the states living along the parametric dimension cannot coexist in the physical system in real space, which limits the potential for investigating crucial physical effects and applications.

One of the approaches to studying EPs in real lattice is to explore NH synthetic dimensions (16). Compared with real NH materials with EPs, such as photonic crystals (17, 18) and waveguide arrays (19, 20), NH synthetic dimensions allow direct observation of the topological phase transitions benefiting from its flexible and dynamic modulation capability. Some inspiring NH phenomena in synthetic lattices including windings and braid (21, 22) of the complex-energy bands in synthetic frequency lattice and NH parity-time time-multiplexed lattice (23) have been investigated. Moreover, synthetic dimensions provide ways to study a high-dimensional system in the low geometric dimensional real systems, such as 4D quantum Hall physics (24) and Weyl physics (25, 26).

In this work, we construct an NH system in a new configuration along the synthetic orbital angular momentum (OAM) dimension (27, 28) in a degenerate cavity. We develop a unique method to explore the band structure along the synthetic OAM dimension, which is referred to as wavefront angle–resolved band structure spectroscopy. We can then directly measure the unique complex spectral features of the EPs, i.e., the existence of bulk Fermi arc, parity time (PT) symmetry breaking transition, the energy swapping when encircling an EP, and half-integer windings of the paired bands. Our results demonstrate the degenerate cavity supporting multiple optical modes that can be used to construct more synthetic dimensions. Moreover, the EPs along the OAM lattice have unique optical applications, such as EP-based angle sensing.

RESULTS

In our system, the even-order OAM, labeled by discrete even-numbered topological charges m ($m \in 2\mathbf{Z}$), is served as a synthetic lattice. The photons with left-hand (↺) and right-hand (↻) circular polarizations carry corresponding spin angular momenta. The coupling between the OAMs and polarizations is introduced by an anisotropic and inhomogeneous medium named Q-plate (29), which has translational symmetry along OAMs because it plays the same operation on all m. The colored doughnut-shaped rings in Fig. 1A represent the corresponding polarized OAM modes. To create a large lattice based on OAM modes, a degenerate optical cavity (30–32), as shown in Fig. 1B, resonantly supporting multiple optical modes, is used to trap the polarized photons carrying OAMs. The operation of Q-plate in terms of spin-orbit coupling in "momentum" space can be expressed as

$$J_Q(k, \delta) = \begin{pmatrix} \cos(\delta/2) & i\sin(\delta/2)e^{-ik} \\ i\sin(\delta/2)e^{ik} & \cos(\delta/2) \end{pmatrix} \quad (1)$$

where k represents the quasi-momentum of the synthetic OAM lattice and δ is the optical retardation controlled by the applied electric field (see Materials and Methods for more details). $\delta \in [-\pi, \pi]$ determines the coupling strength between optical modes, which can

[1]CAS Key Laboratory of Quantum Information, University of Science and Technology of China, Hefei 230026, China. [2]CAS Center For Excellence in Quantum Information and Quantum Physics, University of Science and Technology of China, Hefei 230026, China. [3]Hefei National Laboratory, University of Science and Technology of China, Hefei 230088, China.
*These authors contributed equally to this work.
*Corresponding author. Email: jsxu@ustc.edu.cn (J.-S.X.); smhan@ustc.edu.cn (Y.-J. H.); cfli@ustc.edu.cn (C.-F.L.)
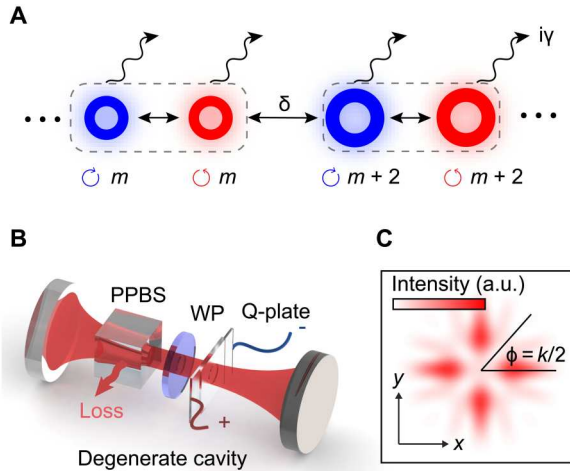
Fig. 1. The synthetic lattice and experimental setup. (**A**) Schematic of synthetic OAM lattice. The OAM modes with topological charge m are marked as the arrays of doughnut-shaped rings. The left (↺) and right (↻) circular polarizations are shown in red and blue, respectively. Arrows represent the interaction (straight) and loss (wavy) of optical modes. The coupling strength between different OAM modes is controlled by the parameter δ, which serves as another synthetic dimension in momentum space. (**B**) The degenerate cavity accommodates multiple OAM modes with different polarizations. The spin-orbital coupling is achieved by repeatedly passing a wave plate (WP), an anisotropic and inhomogeneous medium (Q-plate), which is controlled by electrical fields. A PPBS is used to introduce the non-Hermitian term. (**C**) An example of the average photon transverse distribution from the cavity, which consists of many different polarized OAM modes. The output intensity along quasi-momentum k is obtained by scanning the wavefront angle of $\phi = k/2$, which is referred to as the wavefront angle–resolved band structure spectroscopy. a.u., arbitrary units.

be regarded as an additional pseudomomentum in momentum space.

Generally, the EPs can be obtained by an NH-type perturbation around a Hermitian Dirac point. As shown in Fig. 1B, a quarter-wave plate with the operation $J_{\lambda/4} = e^{i\pi\sigma_x/4}$ on polarizations is introduced into the cavity to construct the Dirac point in the Hermitian realm. λ represents the wavelength of the input photons. Therefore, the evolution of the photon in one period is $\hat{U}(k, \delta) = J_Q(k, \delta)J_{\lambda/4}J_{\lambda/4}J_Q(k, \delta)$. Because of the periodicity of the evolution, the effective Hamiltonian of the system can be obtained by $\hat{H}_{\mathrm{eff}}(k, \delta) = -i\ln\hat{U}(k, \delta)$, which can be simplified as a linear function of the Pauli operators σ_x and σ_y on the parameter space close to $(k, \delta) = (0, -\pi/2)$. The corresponding theoretical band structure is shown in Fig. 2A, in which $(0, -\pi/2)$ is the Dirac point.

The non-Hermitian perturbation around the Dirac point is introduced by a nonunitary operator $J_M = e^{\gamma\sigma_x/2}$, which introduces unbalanced operations on the eigenvectors of σ_x with eigenvalues of $+1$ and -1. γ represents the loss control parameter. Experimentally, the operator J_M is achieved via a partially polarized beam splitter (PPBS) (*33*) as shown in Fig. 1B. It has a high permeability for horizontally polarized $((|\circlearrowright\rangle + |\circlearrowleft\rangle)/\sqrt{2})$ photons. In contrast, only $e^{-\gamma}$ of the photons can be transmitted, and the rest will be reflected out of the cavity (lost) for the vertically polarized $((|\circlearrowright\rangle - |\circlearrowleft\rangle)/\sqrt{2})$ photons. The loss effects in the lattice model are denoted as wavy colors in Fig. 1B.

With the non-Hermitian perturbation J_M, the whole evolution of one round trip in the degenerate cavity is updated to $\hat{U}_{\mathrm{NH}}(k, \delta) = J_Q(k, \delta)J_{\lambda/4}J_MJ_MJ_{\lambda/4}J_Q(k, \delta)$. Similarly, we can obtain the effective Hamiltonian $\hat{H}_{\mathrm{NH}}(k, \delta) = -i\ln\hat{U}_{\mathrm{NH}}(k, \delta)$ around the Dirac point $(0, -\pi/2)$. The detailed expression of $\hat{H}_{\mathrm{NH}}(k, \delta)$ can be found in section SI of the Supplementary Materials, which has complex eigenvalues. Moreover, a pair of EPs with the coalescence of eigenenergies and eigenvectors appear in the quasi-momentum space at $(k, \delta) = [\pm\cos^{-1}(\cosh\gamma)^{-1}, -\pi/2]$. The theoretical simulation result is shown in Fig. 2B. By tuning the parameter γ, the paired EPs would continuously move in the momentum space and can never vanish, except that they meet, indicating the stability of the non-Hermitian phase (*1*). The complex-energy bands of $\hat{H}_{\mathrm{NH}}(k, \delta)$ are subdivided into the real part (Fig. 2C) and imaginary part (Fig. 2D), respectively, in which the bulk Fermi arc and imaginary bulk Fermi (i-Fermi) arc connecting the EPs are also denoted (see section SII for more details).

According to the input-output relationship of the cavity, the complex-energy band can be directly measured through the transmission intensities of the degenerate cavity, from which the unique features of the EPs would be shown. In the experiment, a continuous-wave laser is used to pump the cavity, and the transmission intensities are recorded by scanning the cavity length ΔL. Since the scanning frequency of the cavity length is much smaller than the free spectral range, the system reaches its steady state for each detuning (see section SIII for more details). As discussed in detail in section SIV, the normalized transmission intensity I of the system containing all complex energy information is given by

$$I = \sum_s \frac{\Gamma_0^2}{[\Gamma - \mathrm{Im}(E_s(k, \delta))]^2 + [\beta\Delta L - \mathrm{Re}(E_s(k, \delta))]^2} \quad (2)$$

$\Gamma = \Gamma_0 + \gamma$, and Γ_0 represents the parameter that characterizes the loss of the cavity without the PPBS. $s = \pm 1$ corresponds to the two bands of complex energy $E_s(k, \delta)$, and we use $s = \pm$ in the rest of the description for simplicity. $\beta = 2\pi/\lambda$ represents the wave number. According to Eq. 2, when the real part of complex energy $(\mathrm{Re}[E_\pm(k, \delta)])$ is equal to the cavity detuning $\beta\Delta L$, the output transmission intensity would reach its local maximum I_m. At the same time, the imaginary part of complex energy $\{\mathrm{Im}[E_\pm(k, \delta)]\}$ can be approximatively obtained as $\Gamma - \Gamma_0/\sqrt{I_m}$. The complex energy can then conveniently estimate without any prior information of the energy form. Therefore, the complex band structure can be directly obtained through detecting the transmission intensity spectrum of the cavity.

To obtain the value of $E_\pm(k, \delta)$ along k, we develop a method referred to as the wavefront angle–resolved band structure spectroscopy. Figure 1C displays a representative average photon transverse distribution from the cavity. ϕ represents the azimuth angle parameter of the OAM wavefront in the cylindrical coordinate. The quasi-momentum k in the corresponding reciprocal space of the OAM lattice is physically equal to $\phi/2$, and $0 < \phi < \pi$ can be regarded as a Brillouin zone. The transmission intensity along the quasi-momentum k can be obtained by choosing the photons along angle 2ϕ, from which $E_\pm(k, \delta)$ can then be deduced (see Materials and Methods and section SV for more details).

The experimental and numerical transmission spectra I with $\delta = -\pi/2$ and $\gamma = 0.35$ as a function of $\beta\Delta L$ and k are shown in Fig. 3 (A
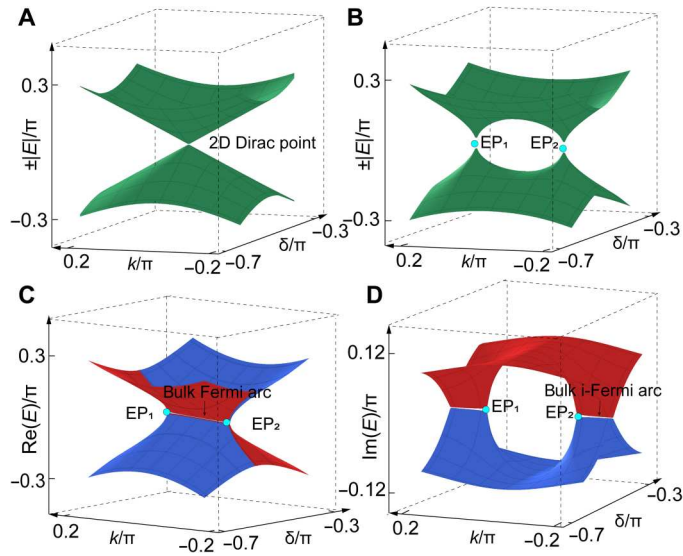
Fig. 2. Theoretical exceptional topological bands by perturbing a Dirac point for γ=0.35. (A) The band structure near Hermitian Dirac point. (**B**) A pair of EPs (EP$_1$ and EP$_2$) appear by introducing a non-Hermitian loss. The EPs are labeled as cyan points. The real (**C**) and imaginary (**D**) parts of the non-Hermitian bands with the EPs are connected by the bulk Fermi arc and bulk i-Fermi arcs, respectively. The bands of $s = +$ and $s = -$ are labeled in red and blue, respectively.

and B, respectively). The experimental results agree with the theoretical predictions. We find that the maximum transmission intensity appears when k locates around zero ($k \in [-0.108\pi, 0.108\pi]$). At the same time, the value of ΔL is equal to zero, which implies that the real part of the complex energy $E_{\pm}(k, -\pi/2)$ degenerates and becomes zero, denoted as a bulk Fermi arc. We further show the transmission signals summing all k in section SVI. The energy band structures can be conveniently engineered by slightly adjusting the cavity (see section SVII for more details).

The experimental result of $\mathrm{Re}[E_{\pm}(k, -\pi/2)]$ is shown in Fig. 3C. Two local maximal of $\mathrm{Re}[E_{\pm}(k, -\pi/2)]$ are found at the region $k \notin [-0.108\pi, 0.108\pi]$, which correspond to the two band structures of the spectrum. Blue and red circles represent the experimental results of $E_{+}(k, -\pi/2)$ and $E_{-}(k, -\pi/2)$, with the blue and red solid lines representing the corresponding theoretical predictions, respectively. Two EPs (EP$_1$ and EP$_2$) denoted as cyan points appear at $k = \pm 0.108\pi$ and are connected by the bulk Fermi arc.

The unique feature can be seen in the imaginary part of the energy bands $\mathrm{Im}[E_{\pm}(k, \delta)]$. The experimental and theoretical results are shown in Fig. 3D. At the region $k \notin [-0.108\pi, 0.108\pi]$, $\mathrm{Im}[E_{\pm}(k, -\pi/2)]$ degenerates and becomes zero, which means that there exists a path connecting two EPs with pure real energy and is denoted as the bulk i-Fermi arc. For the gray region $k \in [-0.108\pi, 0.108\pi]$, because of the overlap of the transmission peaks I_m (the degeneracy of the two real bands), we can only get the imaginary energy of the larger peak from Fig. 3A, which corresponds to the $s = +$ band. When $\mathrm{Re}[E_{\pm}(k, -\pi/2)]$ is zero, the corresponding imaginary parts are nonzero except at EPs, which contribute to the local maximal transmission. The experimental imaginary energy $\mathrm{Im}[E_{+}(k, -\pi/2)]$ gaps at EPs are caused by errors in the estimation of imaginary energy according to local maximum intensities (see section SIV for more details).

With the experimentally measured real and imaginary parts of energy for $s = +$, the results of total absolute value, $|E_{+}| = \sqrt{\mathrm{Re}[E_{+}(k, -\pi/2)]^2 + \mathrm{Im}[E_{+}(k, -\pi/2)]^2}$, are shown in Fig. 3E. The green circles and solid green lines represent the experimental and theoretical results, respectively. The two EPs are directly determined by $|E_{+}| = 0$.

By scanning k, the pure real energy (white region) transmits to the pure imaginary energy (gray region), which corresponds to the phase transition from PT symmetry to PT symmetry breaking regime. The PT breaking transition points are EPs. The eigenvalues [$\Lambda = e^{iE_{\pm}(k, -\pi/2)}$] of the PT-symmetric $\hat{U}_{\mathrm{NH}}$ locate on a unit circle, while for the $\hat{U}_{\mathrm{NH}}$ with PT symmetry breaking, the eigenvalues will locate inside or outside the unit circle. The theoretical prediction of Λ is represented by the yellow ring with a line crossing at the EPs. The experimental results given by the yellow circles in Fig. 3F agree well with the theoretical results.

It is worthy to note the variation of energy $|E_{\pm}(k, -\pi/2)|$ responding nonlinearly with the shift of azimuth angle $\Delta\phi$ (corresponding to the shift momentum $\Delta k/2$) near the EPs. The relationship is denoted as $|E| \propto \sqrt{\Delta\phi}$, which can be used to sense the smaller angle shift and refers to EP-based sensing (see section SVIII for details) (*34*).

The complex energy of a two-band NH system lies on a two-sheeted Riemann surface. As a result, the corresponding eigenenergy will swap as the tuned momenta encircling an EP. The eigenvector, starting in the upper band, will evolve to the lower band after the winding. To demonstrate this feature, we start/end the eigenvector of the system with the energy located on the bulk i-Fermi arc when $(k, \delta) = (-0.6\pi, -0.5\pi)$ (yellow point). The momenta (k, δ) are adiabatically tuned to encircle the EP$_2$ with $(k, \delta) = (-0.108\pi, -0.5\pi)$ (cyan point). The evolution loops are denoted as the white lines in Fig. 4 (A and B) for $\mathrm{Im}[E_{\pm}(k, \delta)]$ and $\mathrm{Re}[E_{\pm}(k, \delta)]$, respectively. The energy bands of $s = +$ and $s = -$ are labeled in red and blue, respectively. We can find that the projected evolution loops on the (k, δ) space encircle the EP$_2$.

For each transmission spectrum of (k, δ), there are two peaks corresponding to the two energy bands with $s = \pm$ (see section SIX). They are distinguishable excepted EPs because of the existence of the energy gap. The typical normalized transmission spectra corresponding to the colored points [start/end (yellow), I (red), II (green), III (purple), and IV (blue)] on the evolution loops are shown in the inset of Fig. 4C. For clarity, we only continuously trace one of the transmission peaks (corresponding to $s = +$) to determine the variation of the complex energy here. The experimental imaginary and real energy are denoted as circles, which are shown in Fig. 4 (C and D, respectively). The arrow lines represent the theoretical loops.

The end point separates from the start point with the energy swapping from $|E_{+}(-0.6\pi, -0.5\pi)|$ to $-|E_{+}(-0.6\pi, -0.5\pi)|$ as encircling the EP$_2$. The observed phenomenon directly demonstrates the unique characteristics of the Riemann surface of the topological energy band.

Moreover, the singularity of Riemann energy surface permits the half-integer windings of the paired bands in the complex-energy plane. The loops shown in Fig. 4 (A and B) can be parametrized by an angle $\theta \in [0, 2\pi]$ around the EP$_2$. The corresponding results of θ in the complex-energy plane are shown in Fig. 4E. The circles are experimental results for the paired bands of $s = +$ (red) and $s = -$
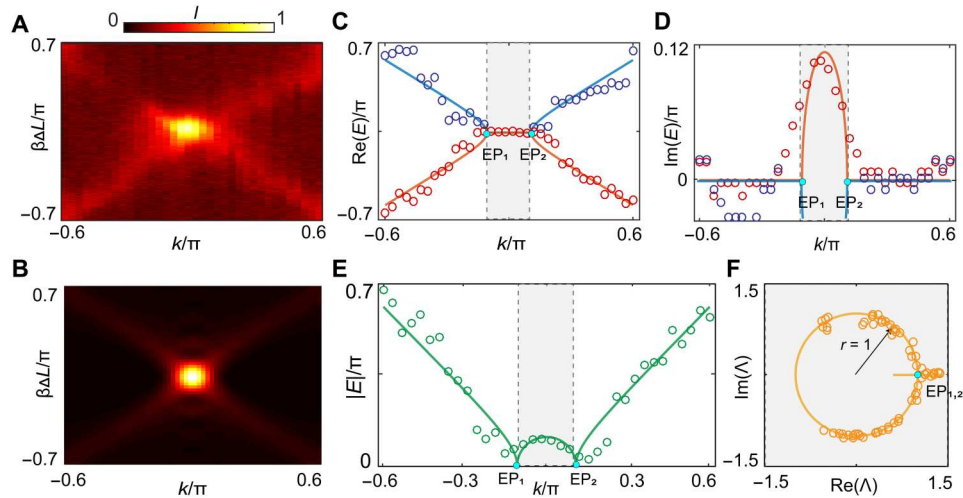
Fig. 3. Observation of EPs and bulk Fermi arcs. (**A**) The experimentally normalized transmission spectrum I when $\delta = -\pi/2$ and $\gamma = 0.35$. (**B**) The theoretical transmission spectrum. (**C**) The real part of complex-energy band $\mathrm{Re}[E_\pm(k, -\pi/2)]$ extracted from the cavity detuning $\beta\Delta L$ corresponding to the local maximum transmission. The EPs are labeled as cyan points. The blue and red circles represent the experimental results of $\mathrm{Re}[E_+(k, -\pi/2)]$ and $\mathrm{Re}[E_-(k, -\pi/2)]$, with the solid blue and red lines representing the theoretical predictions, respectively. The bands of $s = +$ and $s = -$ are labeled in red and blue, respectively. (**D**) The imaginary part of complex-energy band $\mathrm{Im}[E_\pm(k, -\pi/2)]$ extracted from the transmission intensities. The blue and red circles represent the experimental results of $\mathrm{Im}[E_+(k, -\pi/2)]$ and $\mathrm{Im}[E_-(k, -\pi/2)]$, with the solid blue and red lines representing the theoretical predictions, respectively. At the gray region of $k \in [-0.108\pi, 0.108\pi]$, only the results of $\mathrm{Im}[E_+(k, -\pi/2)]$ are shown. (**E**) The absolute value of energy $|E_+| = \sqrt{\mathrm{Re}[E_+(k, -\pi/2)]^2 + \mathrm{Im}[E_+(k, -\pi/2)]^2}$. The green circles and lines represent the experimental and theoretical results, respectively. (**F**) The eigenvalues of the evolution operators $\hat{U}_{\mathrm{NH}}$ in the complex plane. The yellow circle and the line crossing the EPs represent the corresponding theoretical predictions, respectively. The yellow circles represent the experimental results. The deviation away from the unit circle indicates the breaking of the PT symmetry.

(blue). The solid and dashed arrow curves represent the theoretical loop and projection energy trajectories, respectively. It is seen that the winding number of each band is 1/2, which defines a topological invariant associated with the NH band structures (*35*).

DISCUSSION

In summary, we experimentally realize an NH system based on polarized twisted photons in a degenerate cavity and directly obtain the spectral features with respect to EPs. The wavefront angle–resolved band structure spectroscopy for the synthetic OAM lattice is used to directly detect the complex energy and momenta with EPs, which could also be applied in EP-based angle sensing.

Moreover, many more distinguished NH spectra can be investigated along the synthetic OAM dimension, such as the spectra of edge state (*27*, *36*) and the spectra with gauge fields (*28*). In addition, signatures connected with the accumulation of OAM modes would be interesting to investigate as two EPs naturally form a point gap exhibiting the non-Hermitian skin effect (*37*). The degenerate cavity supporting multiple photon degrees of freedom provides the potential to construct multiple synthetic dimensions. In section SX, we preliminarily illustrate this advantage in experiment by introducing an additional independent synthetic frequency and detecting its energy bands in the degenerate cavity.

Our work connects topological photonics, singular optics, and non-Hermitian physics, opening exciting opportunities to explore the topological properties of NH systems. In addition, the cavities with EPs may contribute to new-fashioned multimode laser cavities (*38*, *39*) and to develop a highly sensitive sensor (*10*, *40*). In the future, with the introduction of interphoton interactions, we

believe that synthetic dimensions will have an advantage in simulating numerically difficult large non-Hermitian systems compared with classical computers.

MATERIALS AND METHODS
Operation of Q-plate
In the real space, the operation of Q-plate is described as

$$J_Q(\delta) = \sum_m \cos(\delta/2)(a_{\circlearrowleft,m}^\dagger a_{\circlearrowleft,m} + a_{\circlearrowright,m}^\dagger a_{\circlearrowright,m})$$
$$+ i\sin(\delta/2)(a_{\circlearrowleft,m+2q}^\dagger a_{\circlearrowright,m}^\dagger + \mathrm{h.c.}) \quad (3)$$

where $\circlearrowleft(\circlearrowright)$ represents the left (right) circular polarized modes, m is the topological charge number of OAM mode with corresponding twisted wavefront, $a_{\circlearrowleft(\circlearrowright),m}^\dagger$ [$a_{\circlearrowleft(\circlearrowright),m}$] denotes the corresponding creation (annihilation) operator, δ is the relative optical retardation between $\circlearrowleft$ and $\circlearrowright$ modes in the Q-plate, which can be tuned by the applied electric field. Note that δ can be regarded as an additional pseudomomentum, which introduces another synthetic dimension in momentum space. q is the topological charge number of the Q-plate and $q = 1$ in our experiment. As a result, the OAM transition occurs among even-order modes. It is worth mentioning that the long-range coupling can be controlled by increasing the parameter q.

Because Q-plate has the same operation on different optical modes, the operation J_Q has translational symmetry operation on m. As a result, we can introduce the Bloch mode $|k\rangle = \sum_n e^{-ink}|n\rangle$ ($n = m/2$) in momentum space. The operation can be recast in the "quasi-momentum" space as $J_Q(\delta) = \int_{-\pi}^{\pi} J_Q(k, \delta)dk$, where $J_Q(k, \delta)$ has the form of Eq. 1.
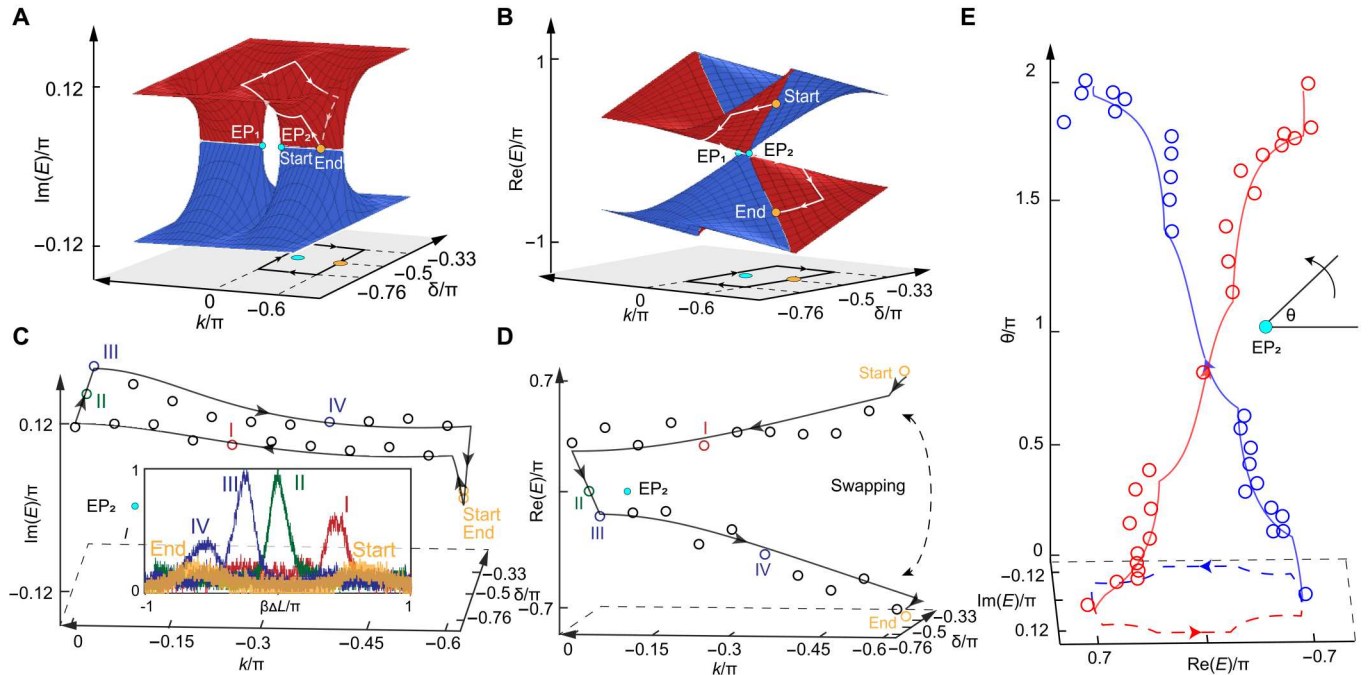
Fig. 4. The swapping of energy when winding around an EP. (**A**) The winding loop on imaginary energy bands. (**B**) The corresponding winding loop on real energy bands. The winding directions in (k, δ) space around EP_2 are as follows: $(-0.6\pi, -0.5\pi) \rightarrow (-0.6\pi, -0.76\pi) \rightarrow (0, -0.76\pi) \rightarrow (0, -0.33\pi) \rightarrow (-0.6\pi, -0.33\pi) \rightarrow (-0.6\pi, -0.5\pi)$. The bands of $s = +$ and $s = -$ are labeled in red and blue, respectively. (**C**) The experimental imaginary part of energy along the loop. Inset: The transmission intensity spectra when (k, δ) are as follows: $(-0.6\pi, -0.5\pi)$ (start and end point, yellow), (I) $(-0.25\pi, -0.76\pi$, red), (II) $(0, -0.5\pi$, green), (III) $(0, -0.33\pi$, purple), and (IV) $(-0.375\pi, -0.33\pi$, blue), which correspond to the colored circles in the evolution loops. The observed peaks correspond to $s = +$. (**D**) The experimental real part of energy along the loop. (**E**) Windings of the paired bands in the complex-energy plane. The angle θ around EP_2 parametrizes the loop, and the bands of $s = +$ and $s = -$ are labeled in red and blue, respectively. The circles represent the experimental results, and the solid arrow curves represent the theoretical energy trajectories. The dashed arrow curves are the projection of the energy trajectories.

Wavefront angle–resolved band structure spectroscopy

The wavefront angle–resolved band structure spectroscopy is an efficient method to probe the complex-energy band along the synthetic OAM dimension, which is inspired by the angle-resolved photoemission spectroscopy used in condensed matter physics. Within the paraxial approximation, the photon wave function $|m\rangle$ carrying even-order OAM with the topological charge of m can be approximately expressed as

$$| m \rangle = E_0(r, \phi)e^{im\phi} \qquad (4)$$

in cylindrical coordinate (r, ϕ). $E_0(r, \phi)$ represents the amplitude. For the lattice consisted by OAMs, the reciprocal Bloch state $| k \rangle = \sum_{n=-\infty}^{n=\infty} e^{-ink} | n \rangle$, where $n = m/2$ represents the number of lattice sites. Hence, the wave function corresponding to $|k\rangle$ can be written as

$$
\begin{aligned}
| k \rangle &= \sum_{n=-\infty}^{n=\infty} e^{-ink} | n \rangle \\
&= E_0(r, \phi) \sum_{n=-\infty}^{n=\infty} e^{-in(k-2\phi)} \qquad (5) \\
&= E_0(r, \phi)\delta(k, 2\phi)
\end{aligned}
$$

which means that we can postselect the output state on the basis of $|k\rangle\langle k|$ by detecting output photons at the angle $\phi = k/2$ through a diaphragm.

Compared with the 2D Fourier transform for the split-step coherent walk to reconstruct the band structure (*41, 42*), the wavefront angle–resolved band structure spectroscopy is an all-optical direct detection method that does not need the tomography process. In the synthetic frequency dimension, the quasi-momentum k is mapped to the time t (*43*). The used time-resolved band structure spectroscopy needs a high-bandwidth photoelectric detector to isolate the momentum k because the first Brillouin zone lived in a very short time interval $[0, T_R]$. T_R is the round-trip time of photons in the cavity, while in our method, the resolution of detected momentum k only relies on the minimal vertex angle of a fan-shaped diaphragm. With the increase of angle resolution, the transmitted light signal will reduce.

REFERENCES AND NOTES

1. E. J. Bergholtz, J. C. Budich, F. K. Kunst, Exceptional topology of non-Hermitian systems. *Rev. Mod. Phys.* **93**, 015005 (2021).

2. W. D. Heiss, The physics of exceptional points. *J. Phys. A* **45**, 444016 (2012).

3. M. A. Miri, A. Alu, Exceptional points in optics and photonics. *Science* **363**, eaar7709 (2019).

4. W. Tang, X. Jiang, K. Ding, Y. X. Xiao, Z. Q. Zhang, C. T. Chan, G. Ma, Exceptional nexus with a hybrid topological invariant. *Science* **370**, 1077–1080 (2020).

5. Y. Wu, W. Liu, J. Geng, X. Song, X. Ye, C. K. Duan, X. Rong, J. F. Du, Observation of parity-time symmetry breaking in a single-spin system. *Science* **364**, 878–880 (2019).

6. B. Hu, Z. Zhang, H. Zhang, L. Zheng, W. Xiong, Z. Yue, X. Wang, J. Xu, Y. Cheng, X. Liu, J. Christensen, Non-Hermitian topological whispering gallery. *Nature* **597**, 655–659 (2021).

7. J. Doppler, A. A. Mailybaev, J. Böhm, U. Kuhl, A. Girschik, F. Libisch, T. J. Milburn, P. Rabl, N. Moiseyev, S. Rotter, Dynamically encircling an exceptional point for asymmetric mode switching. *Nature* **537**, 76–79 (2016).

8. Q. Zhong, M. Khajavikhan, D. N. Christodoulides, R. El-Ganainy, Winding around non-Hermitian singularities. *Nat. Commun.* **9**, 4808 (2018).

9. H. Zhou, C. Peng, Y. Yoon, C. W. Hsu, K. A. Nelson, L. Fu, J. D. Joannopoulos, M. Soljačić, B. Zhen, Observation of bulk Fermi arc and polarization half charge from paired exceptional points. *Science* **359**, 1009–1012 (2018).

10. M. P. Hokmabadi, A. Schumer, D. N. Christodoulides, M. Khajavikhan, Non-Hermitian ring laser gyroscopes with enhanced Sagnac sensitivity. *Nature* **576**, 70–74 (2019).

11. H. Hodaei, A. U. Hassan, S. Wittek, H. Garcia-Gracia, R. El-Ganainy, D. N. Christodoulides, M. Khajavikhan, Enhanced sensitivity at higher-order exceptional points. *Nature* **548**, 187–191 (2017).

12. W. Liu, Y. Wu, C. Duan, X. Rong, J. Du, Dynamically encircling an exceptional point in a real quantum system. *Phys. Rev. Lett.* **126**, 170506 (2021).

13. H. Hodaei, M.-A. Miri, M. Heinrich, D. N. Christodoulides, M. Khajavikhan, Parity-time-symmetric microring lasers. *Science* **346**, 975–978 (2014).

14. L. Feng, Z. J. Wong, R. M. Ma, Y. Wang, X. Zhang, Single-mode laser by parity-time symmetry breaking. *Science* **346**, 972–975 (2014).

15. X. Zhang, K. Ding, X. Zhou, J. Xu, D. Jin, Experimental observation of an exceptional surface in synthetic dimensions with magnon polaritons. *Phys. Rev. Lett.* **123**, 237202 (2019).

16. L. Yuan, Q. Lin, M. Xiao, S. Fan, Synthetic dimension in photonics. *Optica* **5**, 1396–1405 (2018).

17. K. H. Kim, M. S. Hwang, H. R. Kim, J. H. Choi, Y. S. No, H. G. Park, Direct observation of exceptional points in coupled photonic-crystal lasers with asymmetric optical gains. *Nat. Comm.* **7**, 13893 (2016).

18. B. Zhen, C. W. Hsu, Y. Igarashi, L. Lu, I. Kaminer, A. Pick, S. L. Chua, J. D. Joannopoulos, M. Soljačić, Spawning rings of exceptional points out of Dirac cones. *Nature* **525**, 354–358 (2015).

19. A. Cerjan, S. Huang, M. Wang, K. P. Chen, Y. Chong, M. C. Rechtsman, Experimental realization of a Weyl exceptional ring. *Nat. Photo.* **13**, 623–628 (2019).

20. J. W. Yoon, Y. Choi, C. Hahn, G. Kim, S. H. Song, K. Y. Yang, J. Y. Lee, Y. Kim, C. S. Lee, J. K. Shin, H. S. Lee, P. Berini, Time-asymmetric loop around an exceptional point over the full optical communications band. *Nature* **562**, 86–90 (2018).

21. K. Wang, A. Dutt, K. Y. Yang, C. C. Wojcik, J. Vučković, S. Fan, Generating arbitrary topological windings of a non-Hermitian band. *Science* **371**, 1240–1245 (2021).

22. K. Wang, A. Dutt, C. C. Wojcik, S. Fan, Topological complex-energy braiding of non-Hermitian bands. *Nature* **598**, 59–64 (2021).

23. A. Regensburger, C. Bersch, M. A. Miri, G. Onishchukov, D. N. Christodoulides, U. Peschel, Parity-time synthetic photonic lattices. *Nature* **488**, 167–171 (2012).

24. M. Lohse, C. Schweizer, H. M. Price, O. Zilberberg, I. Bloch, Exploring 4D quantum Hall physics with a 2D topological charge pump. *Nature* **553**, 55–58 (2018).

25. Z. W. Yan, Q. Wang, M. Xiao, Y. L. Zhao, S. N. Zhu, H. Liu, Probing rotated Weyl physics on nonlinear lithium niobate-on-insulator chips. *Phys. Rev. Lett.* **127**, 013901 (2021).

26. Q. Wang, M. Xiao, H. Liu, S. Zhu, C. T. Chan, Optical interface states protected by synthetic Weyl points. *Phys. Rev. X* **7**, 031032 (2017).

27. M. Yang, H. Q. Zhang, Y. W. Liao, Z. H. Liu, Z. W. Zhou, X. X. Zhou, J. S. Xu, Y. J. Han, C. F. Li, G. C. Guo, Topological band structure via twisted photons in a degenerate cavity. *Nat. Commun.* **13**, 2040 (2022).

28. X. W. Luo, X. Zhou, C. F. Li, J. S. Xu, G. C. Guo, Z. W. Zhou, Quantum simulation of 2D topological physics in a 1D array of optical cavities. *Nat. Commun.* **6**, 7704 (2015).

29. L. Marrucci, C. Manzo, D. Paparo, Optical spin-to-orbital angular momentum conversion in inhomogeneous anisotropic media. *Phys. Rev. Lett.* **96**, 163905 (2006).

30. Z. D. Cheng, Z. D. Liu, X. W. Luo, Z. W. Zhou, J. Wang, Q. Li, Y. T. Wang, J. S. Tang, J. S. Xu, C. F. Li, G. C. Guo, Degenerate cavity supporting more than 31 Laguerre Gaussian modes. *Opt. Lett.* **42**, 2042–2045 (2017).

31. Z. D. Cheng, Q. Li, Z. H. Liu, F. F. Yan, S. Yu, J. S. Tang, Z. W. Zhou, J. S. Xu, C. F. Li, G. C. Guo, Experimental implementation of a degenerate optical resonator supporting more than 46 Laguerre-Gaussian modes. *Appl. Phys. Lett.* **112**, 201104 (2018).

32. Z. D. Cheng, Z. H. Liu, Q. Li, Z. W. Zhou, J. S. Xu, C. F. Li, G. C. Guo, Flexible degenerate cavity with ellipsoidal mirrors. *Opt. Lett.* **44**, 5254–5257 (2019).

33. L. Xiao, X. Zhan, Z. H. Bian, K. K. Wang, X. Zhang, X. P. Wang, J. Li, K. Mochizuki, D. Kim, N. Kawakami, W. Yi, H. Obuse, B. C. Sanders, P. Xue, Observation of topological edge states in parity-time-symmetric quantum walks. *Nat. Phys.* **13**, 1117–1123 (2017).

34. J. Wiersig, Review of exceptional point-based sensors. *Photon. Res.* **8**, 1457–1467 (2020).

35. H. Shen, B. Zhen, L. Fu, Topological band theory for non-Hermitian Hamiltonians. *Phys. Rev. Lett.* **120**, 146402 (2018).

36. X. F. Zhou, X. W. Luo, S. Wang, G. C. Guo, X. Zhou, H. Pu, Z. W. Zhou, Dynamically manipulating topological physics and edge modes in a single degenerate optical cavity. *Phys. Rev. Lett.* **118**, 083603 (2017).

37. N. Okuma, K. Kawabata, K. Shiozaki, M. Sato, Topological origin of non-Hermitian skin effects. *Phys. Rev. Lett.* **124**, 086801 (2020).

38. M.-A. Miri, P. LiKamWa, D. N. Christodoulides, Large area single-mode parity-time-symmetric laser amplifiers. *Opt. Lett.* **37**, 764–766 (2012).

39. H. Wenzel, U. Bandelow, H.-J. Wunsche, J. Rehberg, Mechanisms of fast self pulsations in two-section DFB lasers. *IEEE J. Quantum Electron.* **32**, 69–78 (1996).

40. Y.-H. Lai, Y.-K. Lu, M.-G. Suh, Z. Yuan, K. Vahala, Observation of the exceptional-point-enhanced Sagnac effect. *Nature* **576**, 65–69 (2019).

41. S. Weidemann, M. Kremer, S. Longhi, A. Szameit, Topological triple phase transition in non-Hermitian Floquet quasicrystals. *Nature* **601**, 354–359 (2022).

42. A. F. Adiyatullin, L. K. Upreti, C. Lechevalier, C. Evain, F. Copie, P. Suret, S. Randoux, P. Delplace, A. Amo, Multi-topological Floquet metals in a photonic lattice. arXiv 2203.01056 [physics.optics] (2022).

43. A. Dutt, M. Minkov, Q. Lin, L. Yuan, D. A. B. Miller, S. Fan, Experimental band structure spectroscopy along a synthetic dimension. *Nat. Commun.* **10**, 3122 (2019).

44. J. A. Arnaud, Degenerate optical cavities. *Appl. Optics* **8**, 189–196 (1969).

45. J. A. Arnaud, Degenerate optical cavities. II: Effect of misalignments. *Appl. Opt.* **8**, 1909–1917 (1969).

46. S. H. Murshid, *Optical Fiber Multiplexing and Emerging Techniques* (Morgan & Claypool Publishers, 2018).

47. J. K. Poon, J. Scheuer, Y. Xu, A. Yariv, Designing coupled-resonator optical waveguide delay lines. *JOSA B* **21**, 1665–1673 (2004).

48. I. Chremmos, N. Uzunoglu, Modes of the infinite square lattice of coupled microring resonators. *J. Opt. Soc. Am. A Opt. Image Sci. Vis.* **25**, 3043–3050 (2008).

49. L. Yuan, Q. Lin, A. Zhang, M. Xiao, X. Chen, S. Fan, Photonic gauge potential in one cavity with synthetic frequency and orbital angular momentum dimensions. *Phys. Rev. Lett.* **122**, 083903 (2019).